SECOND EDITION

Characterization of MATERIALS

Volume 3

EDITED BY

Elton N. Kaufmann

WILEY

CHARACTERIZATION OF MATERIALS

SECOND EDITION

Volume 3

Editor-in-Chief

Elton N. Kaufmann
Argonne National Laboratory
Argonne, IL

Characterization of Materials is available Online in full color at www.mrw.interscience.wiley.com/com.

A JOHN WILEY & SONS, INC., PUBLICATION

Published by John Wiley & Sons, Inc., Hoboken, New Jersey.
Published simultaneously in Canada.

Library of Congress Cataloging-in-Publication Data:
Characterization of materials / edited by Elton N. Kaufmann, Argonne National Laboratory, Argonne, IL. – Second edition.
volumes cm
First edition published as a two volume set, ©2003.
Includes bibliographical references and index.
ISBN 978-1-118-11074-4 (3 volume set)
1. Materials–Research. 2. Materials–Testing. I. Kaufmann, Elton N.
TA404.2.C48 2012
620.1'10287–dc23

2012012521

Printed in the United States of America

10 9 8 7 6 5 4 3 2 1

CHARACTERIZATION OF MATERIALS

EDITOR-IN-CHIEF

Elton N. Kaufmann
Argonne National Laboratory
Argonne, IL

CHAPTER EDITORS

Reza Abbaschian
University of California
Riverside, CA

Peter A. Barnes
Clemson University
Clemson, SC

Andrew B. Bocarsly
Princeton University
Princeton, NJ

Chia-Ling Chien
Johns Hopkins University
Baltimore, MD

Lawrence P. Cook
The Catholic University of America
Washington DC

Alan I. Goldman
Iowa State University
Ames, IA

Joseph P. Hornak
Rochester Institute of Technology
Rochester, NY

Chris Jeynes
University of Surrey
Guildford, UK

Stephen J. Pennycook
Oak Ridge National Laboratory
Oak Ridge, TN

Alan C. Samuels
Edgewood Chemical Biological Center
Aberdeen Proving Ground, MD

Juan M. Sanchez
The University of Texas at Austin
Austin, TX

Alexander Schwarz
Universität Hamburg
Hamburg, Germany

EDITORIAL STAFF

VP & Director, STMS Book Publishing: Janet Bailey
Executive Editor: Arza Seidel
Development Editor: Mihai Peterca
Production Manager: Shirley Thomas
Production Editor: Kristen Parrish
Illustration Editor: Dean Gonzalez

ELECTRON TECHNIQUES

11

STEPHEN J. PENNYCOOK, Chapter Editor

Oak Ridge National Laboratory, Materials Science and Technology Division, Oak Ridge, TN, USA

CONTENTS, VOLUMES 1, 2, AND 3

ELECTRON TECHNIQUES, INTRODUCTION

Electrons are highly versatile probes of materials because they are easily accelerated, readily focused by electromagnetic fields, and they interact strongly with matter. At low energies, they interact with materials surfaces, whereas at high energy, they can probe the bulk (at least the interior of a thin specimen). In addition, at high energies, they have very short wavelengths, for example, 3.7 pm when accelerated to 100 kV, and, given atomic spacings in materials, are 100–200 pm, in principle, fast electrons are easily capable of providing atomic resolution images. Electrons also lose energy to atomic excitations, bringing another plethora of spectroscopic techniques for analysis of surfaces and bulk compositions and electronic structure. This chapter provides overviews of the key methods developed to exploit these characteristics of electrons to probe the structure, composition and chemical bonding of materials, their internal microstructure, and the nature of their surfaces and interfaces.

Transmission electron microscopy is perhaps the most well-known technique for imaging a material's microstructure. The technique requires the sample to be thinned typically to 100 nm or below and can give resolution nowadays to 50 pm, a feat only recently achieved through a major breakthrough in the field, viz., aberration correction. The electromagnetic lenses used as the primary focusing elements in electron microscopes have intrinsic aberrations that are relatively much stronger than we are used to with glass lenses, due to the forms of fields used. For most of the history of the electron microscope, these aberrations meant that lens apertures had to be restricted to angles of just a few degrees, limiting resolution to the order of 100 wavelengths or so. In the past decade, however, thanks to development of fast computers and charge-coupled-device detectors, schemes have been developed to compensate for the intrinsically high aberrations of the round magnetic lens with arrays of multipole lenses. Resolution has improved dramatically, and atomic resolution is now relatively routine, bringing clear new views of materials at the atomic scale. Transmission electron microscopy can use either a fixed beam, when the transmitted electrons are focused onto a viewing screen or imaging detector, or a scanning mode, when images are formed sequentially using various kinds of detectors.

The scanning electron microscope provides views of materials surfaces by scanning a probe across the surface and collecting backscattered and secondary electrons generated near the surface, providing informative views of surface morphology. Because of the small aperture necessary with electron lenses, it has a large depth of field and at the same time a resolution that can exceed optical resolution by orders of magnitude.

Both the transmission and scanning microscopes can be fitted with x-ray detectors to provide quantitative elemental analysis capabilities. In addition, the transmission microscopes can also analyze the energy lost by the electrons as they pass though the specimen. These electron energy loss spectra give information not only on composition, but, as with x-ray absorption spectroscopy, fine structure on the absorption edges can give detailed information on electronic states and bonding in the sample.

True surface-sensitive techniques are available by lowering the beam voltage, as in the case of low-energy electron microscopy, or by using low angles of incidence as with reflection high-energy electron diffraction. Both techniques are sensitive to surface features such as islands or steps, the former providing an image, the latter diffraction analysis. Auger electron spectroscopy is another surface-sensitive technique that probes surface composition and bonding.

This chapter also includes recent notable advances, for example, the capability for fast time resolution with the dynamic transmission electron microscope, advances in imaging with spin-polarized electrons, fluctuation microscopy for analysis of short-range order in disordered and amorphous materials, and in situ electron microscopy for imaging in ambient atmospheres and at temperature, important in catalysis and for studying phase transformations. It is also possible to probe the magnetic state of a material through Lorentz microscopy. We hope that this chapter provides a perspective on the broad range of techniques available that use electron beams and on their applications and insights into materials they can provide.

STEPHEN J. PENNYCOOK
Oak Ridge National Laboratory
Materials Science and Technology Division
Oak Ridge, TN, USA

TRANSMISSION ELECTRON MICROSCOPY

JAMES M. HOWE,[1] BRENT FULTZ,[2] AND SHU MIAO[3]
[1]University of Virginia, Charlottesville, VA, USA
[2]California Institute of Technology, Pasadena, CA, USA
[3]Dalian Institute of Chemical Physics, Dalian, China

INTRODUCTION

Transmission electron microscopy (TEM) is the premier tool for understanding the internal microstructure of materials at the subnanometer level. Electrons can be easily focused using electromagnetic lenses, allowing real-space images of materials with resolutions of a few tenths to a few nanometers, depending on the imaging conditions, and simultaneously obtain diffraction

information from subnanometer regions in the images. Variations in the intensity of electron scattering across a thin specimen can be used to image strain fields, defects such as dislocations and second-phase particles, and even atomic columns in materials under certain imaging conditions. Transmission electron microscopy is such a powerful tool for the characterization of materials that some microstructural features are defined in terms of their visibility in TEM images.

In addition to diffraction and imaging, the high-energy electrons (usually in the range of 100–400 keV of kinetic energy) in TEM cause electronic excitations of the atoms in the specimen. Two important spectroscopic techniques make use of these excitations by incorporating suitable detectors into the transmission electron microscope.

1. In energy-dispersive x-ray spectroscopy (EDS), an x-ray spectrum is collected from small regions of the specimen illuminated with a focused electron probe using a solid-state detector. Characteristic x-rays of each element are used to determine the concentrations of the different elements present in the specimen (Williams and Carter, 2009). The principles behind this technique are discussed in details (see article ENERGY-DISPERSIVE SPECTROMETRY).
2. In electron energy loss spectroscopy (EELS), a magnetic prism is used to separate the electrons according to their energy losses after having passed through the specimen (Egerton, 2011). Energy loss mechanisms such as plasmon excitations and core-electron excitations cause distinct features in EELS. These can be used to quantify the elements present as well as provide information about atomic bonding and a variety of other useful phenomena.

In scanning transmission electron microscopy (STEM), a focused beam of electrons (typically <1 nm in diameter) is scanned in a television-style raster pattern across the specimen, as in a scanning electron microscope (see article SCANNING ELECTRON MICROSCOPY). In synchronization with the raster scan, emissions resulting from the interaction of the electron beam with the specimen are collected, such as x-rays or secondary or backscattered electrons, to form images. Electrons that pass through the specimen can also be detected to form images that are similar to conventional TEM images. An annular detector can be used to collect the scattered transmitted electrons, which leads to Z-contrast imaging (discussed in SCANNING TRANSMISSION ELECTRON MICROSCOPY: Z-CONTRAST IMAGING). The STEM mode of operation is particularly useful for spectroscopic analysis, since it permits the acquisition of a chemical map of the sample typically with a resolution of a few nanometers. For example, one can make an image of the distribution of Fe in a sample by recording, in synchronization with the raster pattern, either the emission from the sample of Fe K_α x rays (with the EDS spectrometer) or transmitted electrons with energy losses greater than that of the Fe L edge (with the EELS spectrometer). The STEM mode of operation is different from the conventional TEM mode in that the objective lens is operated in tandem with the illumination lens system to assist in the formation of a focused electron probe on the specimen (Keyse et al., 1998).

A fully equipped transmission electron microscope has the capability to record the variations in image intensity across the specimen using mass thickness or diffraction contrast techniques, to reveal the atomic structure of materials using high-resolution (phase-contrast) imaging or Z-contrast (incoherent) imaging, to obtain electron diffraction patterns from small areas of the specimen using a selected-area aperture or a focused electron probe, and to perform EELS and EDS measurements with a small probe. Additional lenses can be installed in conjunction with an EELS spectrometer to create an energy filter, enabling one to form energy-filtered TEM images (EFTEM—Krivanek et al., 1987; Reimer, 1995). These images enable mapping of the chemical composition of a specimen with nanometer spatial resolution. A block diagram of such a transmission electron microscope is shown in Figure 1.

In addition to the main techniques of (1) conventional imaging, (2) phase-contrast imaging, (3) Z-contrast imaging, (4) electron diffraction, (5) EDS, and (6) EELS, in TEM many other analyses are possible. For example,

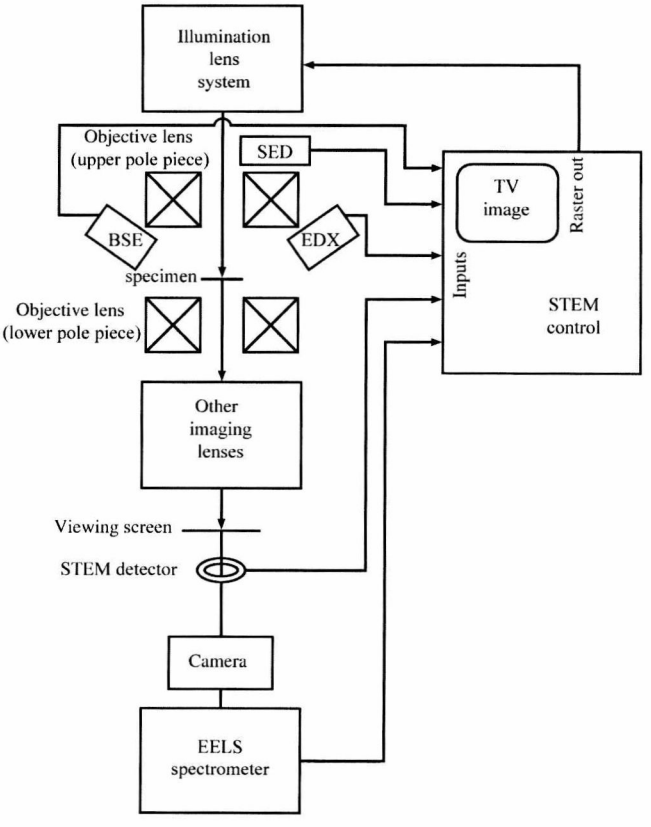

Figure 1. Typical transmission electron microscope with STEM capability. It is also possible to perform scanning electron microscopy (SEM) in a STEM using backscattered electron (BSE) and secondary electron detectors (SED) located above the specimen.

when electrons pass through a magnetic specimen, they are deflected slightly by Lorentz forces, which change direction across a magnetic domain wall. In a method known as Lorentz microscopy (see article LORENTZ MICROSCOPY), special adjustments of lens currents permit imaging of these domain walls (Thomas and Goringe, 1979). Phase transformations and microstructural changes in a specimen can be observed directly as the specimen is heated, cooled, or deformed in the microscope using various specimen stages (Butler and Hale, 1981). Differential pumping can be used to allow the introduction of gases into the microscope column surrounding a thin foil, making it possible to follow chemical reactions in TEM *in situ* (see article *IN SITU* TEM MEASUREMENT METHODS). Cryoelectron microscopy (cryo-EM), an important technique for observing liquid/hydrated materials, uses frozen samples at cryogenic temperatures. Keeping samples frozen helps eliminate radiation damage and protects them from deformation due to dehydration in vacuum. Many of these techniques can be performed at spatial resolutions of a few tenths of a nanometer. The possibilities are almost endless, and that is why TEM continues to be an indispensable tool in materials research. Since it is not possible to cover all of these techniques, this article focuses on the theory and practice of conventional TEM electron diffraction and imaging techniques, with introductions to the commonly used spectroscopic techniques (EDS and EELS) and the fast-growing aberration-corrected high resolution electron microscopy.

A few imaging and diffraction techniques offer the resolution and versatility of TEM and are competitive or complementary in some respects. Transmission electron microscopy is not able to readily image single point defects in materials. In contrast, the field ion microscope (FIM) can be used to study vacancies and surface atoms and therefore extends the available resolution to atomic dimensions (Miller and Smith, 1989). When combined with a mass spectrometer, the FIM becomes an atom probe (APFIM), easily capable of compositional analysis of regions $\sim$1 nm wide and now approaching atom-by-atom analysis of local areas of samples. In the FIM, a high potential is applied to a very fine pointed specimen. A low pressure of inert gas is maintained between the specimen and imaging screen/spectrometer. Positively charged gas ions generated by the process of field ionization are used to produce images of the atoms on the surface of the specimen. Successive atom layers of material may be ionized and removed from the specimen surface by the process of field evaporation, enabling the three-dimensional (3D) structure of the material to be imaged in atomic detail and also to provide the source of ions for mass spectrometry (for more information about FIM, see article ATOM PROBE TOMOGRAPHY and FIELD ION MICROSCOPY).

Another instrument capable of imaging the internal structure of materials is the scanning acoustic microscope (SAM). In this microscope, a lens is used to focus the acoustic emission from an ultrasonic transducer onto a small region of a specimen through a coupling medium such as water. The same lens can be used to collect the acoustic echo from defects below the surface of the specimen. Either the lens or the specimen is scanned mechanically to form a two-dimensional (2D) image, the resolution of which depends on the wavelength of the acoustic wave in the specimen and thus on the frequency of the ultrasound and the velocity of sound in the specimen. Since the depth to which sound waves can penetrate decreases as their frequency increases, the choice of frequency depends on a compromise between resolution and penetration. Typical values might be a resolution of 40–100 μm at a depth of 5 mm below the surface for 50-MHz frequency, or a resolution of 1–3 μm at a similar depth for a frequency of 2 GHz. The resolution is clearly not as good as in TEM although the depth penetration is greater.

Lastly, x-ray diffraction and microscopy (see Chapter X-RAY TECHNIQUES) are alternative techniques to TEM and offer the advantage of greater penetration through materials. The main obstacle to high spatial resolution in both techniques is the difficulty of focusing x-ray beams, since x-rays are uncharged and cannot be focused by electromagnetic or electrostatic lenses. While x-ray diffraction is commonly used for characterization of bulk samples in materials science and can be used to determine the atomic structures of materials (McKie and McKie, 1986), x-ray microscopy is not common, largely due to the better resolution and versatility of TEM.

PRINCIPLES OF THE METHOD

Here we develop the theoretical basis necessary to understand and quantify the formation of diffraction patterns and images in TEM. The theory developed is known as the "kinematical theory" of electron diffraction, and the contrast that arises in TEM images due to electron diffraction is "diffraction contrast." These concepts are then utilized in examples of the method and data analyses.

Structure Factor and Shape Factor

In both real space and in reciprocal space, it is useful to divide a crystal into parts according to the formula (Fultz and Howe, 2008)

$$\mathbf{r} = \mathbf{r_g} + \mathbf{r_k} + \delta\mathbf{r_{g,k}} \tag{1}$$

For a defect-free crystal the atom positions $\mathbf{R}$ are given by

$$\mathbf{R} = \mathbf{r_g} + \mathbf{r_k} \tag{2}$$

where the lattice is one of the 14 Bravais lattice types (see article SYMMETRY IN CRYSTALLOGRAPHY) and the basis is the atom group associated with each lattice site (Borchardt-Ott, 1995). Here we calculate the scattered wave $\psi(\Delta\mathbf{k})$ for the case of an infinitely large, defect-free lattice with a basis:

$$\psi(\Delta\mathbf{k}) = \sum_{\mathbf{R}} f_{at}(\mathbf{R})\exp(-i2\pi\Delta\mathbf{k}\cdot\mathbf{R}) \tag{3}$$

where the scattered wave vector $\Delta\mathbf{k}$ is defined as the difference between the diffracted wave vector $\mathbf{k}$ and the

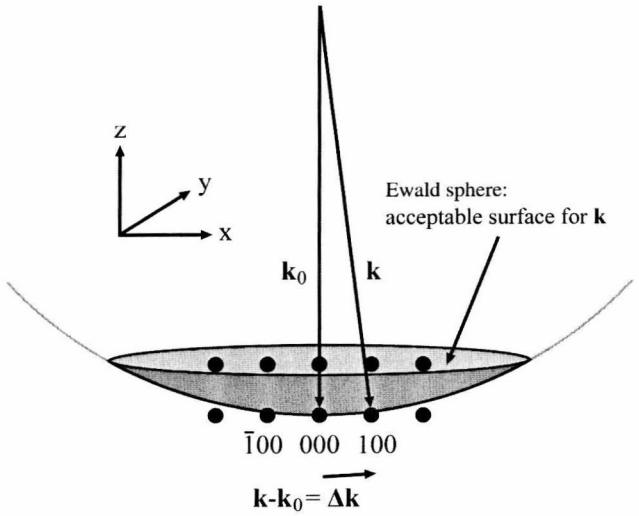

Figure 2. Ewald sphere construction showing incident $\mathbf{k}_0$ and scattered $\mathbf{k}$ wave vectors joined tail to tail and definition of $\Delta\mathbf{k}$.

incident wave vector $\mathbf{k}_0$ (refer to Fig. 2), or

$$\Delta\mathbf{k} = \mathbf{k} - \mathbf{k}_0 \tag{4}$$

and $f_{at}(\mathbf{R})$ is the atomic scattering factor for electrons from an atom. We decompose our diffracted wave into a lattice component and a basis component with

$$\psi(\Delta\mathbf{k}) = \sum_{\mathbf{r_g}+\mathbf{r_k}} f_{\text{at}}(\mathbf{r_g}+\mathbf{r_k})\exp\left[-i2\pi\Delta\mathbf{k}\cdot(\mathbf{r_g}+\mathbf{r_k})\right] \tag{5}$$

Since the atom positions in all unit cells are identical, $f_{\text{at}}(\mathbf{r_g}+\mathbf{r_k})$ cannot depend on $\mathbf{r_g}$, so $f_{\text{at}}(\mathbf{r_g}+\mathbf{r_k}) = f_{\text{at}}(\mathbf{r_k})$, and thus

$$\psi(\Delta\mathbf{k}) = \sum_{\mathbf{r_g}}\exp(-i2\pi\Delta\mathbf{k}\cdot\mathbf{r_g})\sum_{\mathbf{r_k}} f_{at}(\mathbf{r_k})\exp(-i2\pi\Delta\mathbf{k}\cdot\mathbf{r_k}) \tag{6}$$

or, simplifying,

$$\psi(\Delta\mathbf{k}) = \mathcal{S}(\Delta\mathbf{k})\mathcal{F}(\Delta\mathbf{k}) \tag{7}$$

In writing Equation 7, we have given formal definitions to the two summations in Equation 6. The first sum, which is over all the lattice sites of the crystal (all unit cells), is known as the shape factor $\mathcal{S}$. The second sum, which is over the atoms in the basis (all atoms in the unit cell), is known as the structure factor $\mathcal{F}$. The notation($\Delta\mathbf{k}$) is used to indicate the dependence of these terms on $\Delta\mathbf{k}$. The decomposition of the diffracted wave into the shape factor and the structure factor parallels the decomposition of the crystal into a lattice plus a basis.

Calculation of the structure factor $\mathcal{F}(\Delta\mathbf{k})$ for a unit cell is discussed in detail in article KINEMATIC DIFFRACTION OF X-RAYS and in standard books on diffraction (Schwartz and Cohen, 1987) and is not developed further here. Because in TEM we examine thin foils often containing small particles with different shapes, it is useful to examine the shape factor $\mathcal{S}(\Delta\mathbf{k})$ in Equations 6 and 7 in further detail. The shape factor $\mathcal{S}(\Delta\mathbf{k})$ is not very interesting for an infinitely large crystal where it becomes a set of delta functions centered at the various values of $\Delta\mathbf{k}$, where $\Delta\mathbf{k} = \mathbf{g}$ ($\mathbf{g}$ is a reciprocal lattice vector), but it is interesting for small crystals, which give rise to various spatial distributions of the diffracted electron intensity. The full 3D expression for the kinematical diffracted intensity due to the shape factor of a rectangular prism is

$$\mathcal{S}^*\mathcal{S}(\Delta\mathbf{k}) = \frac{\sin^2(\pi\Delta k_x a_x N_x)}{\sin^2(\pi\Delta k_x a_x)}\frac{\sin^2(\pi\Delta k_y a_y N_y)}{\sin^2(\pi\Delta k_y a_y)}\frac{\sin^2(\pi\Delta k_z a_z N_z)}{\sin^2(\pi\Delta k_z a_z)} \tag{8}$$

where a_x, a_y, and a_z are the magnitudes of the primitive translation vectors of the unit cell expressed along orthonormal x, y, and z axes; N_x, N_y, and N_z are the number of unit cells along the same axes, that is, $a_x N_x = t_x$, the crystal thickness along the x direction and similarly for y and z; and Δk_x, Δk_y, and Δk_z are the components of $\Delta\mathbf{k}$ expressed along the x, y, and z axes.

The function in Equation 8 becomes large when the denominator goes to zero. This occurs when the argument of the sine function is equal to π or to some integral multiple of it, expressed (in the x direction only) as

$$\Delta k_x a_x = \text{integer} \tag{9}$$

Since similar conditions are expected for y and z, this condition requires that $\Delta\mathbf{k}$ is a reciprocal lattice vector $\mathbf{g}$. In other words, the kinematical intensity $\mathcal{S}^*\mathcal{S}$ is large when the Bragg condition is exactly satisfied. Since the denominator varies slowly with respect to the numerator, we can make the following approximation, which is valid near the center of the main peaks (expressed in only one direction):

$$\mathcal{S}^*\mathcal{S}(\Delta\mathbf{k}) \cong \frac{\sin^2(\pi\Delta kaN)}{(\pi\Delta ka)^2} \tag{10}$$

This function describes an envelope of satellite peaks situated near the main Bragg diffraction peaks. By examining the numerator, we see that the positions of the satellite peaks get closer to the main peak in proportion to $1/Na$, and the position of the first minimum in the intensity is located on either side of the main peak at the position $\Delta k = 1/Na$. Similarly, the widths of the main peaks and satellite peaks also decrease as $1/Na$. Thus, large crystal dimensions in real space lead to sharp diffracted intensities in reciprocal space, and vice versa (Hirsch et al., 1977; Thomas and Goringe, 1979).

Ewald Sphere Construction

The Bragg condition for diffraction, $\Delta\mathbf{k} = \mathbf{g}$, where $\mathbf{g}$ is a reciprocal lattice vector and $\Delta\mathbf{k}$ is any possible scattered wave vector, can be implemented in a geometrical construction due to Ewald (McKie and McKie, 1986). The Ewald sphere depicts the incident wave vector $\mathbf{k}_0$ and all possible $\mathbf{k}$ for the diffracted waves. The tip of the wave vector $\mathbf{k}_0$ is always placed at a point of the reciprocal lattice that serves as the origin. To obtain $\Delta\mathbf{k} = \mathbf{k} - \mathbf{k}_0$,

we would normally reverse the direction of $\mathbf{k}_0$ and place it tail to head with the vector $\mathbf{k}$, but in the Ewald sphere construction in Figure 2, we draw $\mathbf{k}$ and $\mathbf{k}_0$ tail to tail. The vector $\Delta\mathbf{k}$ is the vector from the head of $\mathbf{k}_0$ to the head of $\mathbf{k}$. If the head of $\mathbf{k}$ touches any reciprocal lattice point, the Bragg condition ($\Delta\mathbf{k} = \mathbf{k} - \mathbf{k}_0$) is satisfied and diffraction occurs. In elastic scattering, the length of $\mathbf{k}$ equals the length of $\mathbf{k}_0$, since there is no change in wavelength (magnitude of the wave vector). The tips of all possible $\mathbf{k}$ vectors lie on a sphere whose center is at the tails of $\mathbf{k}$ and $\mathbf{k}_0$. By this construction, one point on this sphere always touches the origin of the reciprocal lattice. Whenever another point on the Ewald sphere touches a reciprocal lattice point, the Bragg condition is satisfied and diffraction occurs. As illustrated in Figure 2, the Bragg condition is approximately satisfied for the (100) and (100) diffraction spots.

The Ewald sphere is strongly curved for x-ray diffraction because $|\mathbf{g}|$ (typically 5–10 nm^{-1}) is comparable to $|\mathbf{k}_0|$. Electron wave vectors, on the other hand, are much longer than the spacings in the reciprocal lattice (100-keV electrons have a wavelength of 0.0037 nm). So, for high-energy electrons, the Ewald sphere is approximately a plane, and consequently, $\Delta\mathbf{k}$ is nearly perpendicular to $\mathbf{k}_0$. In practice, the diffracted intensity distribution, such as that in Equation 8, is located in a finite volume around the reciprocal lattice points, so $\Delta\mathbf{k}$ need not equal $\mathbf{g}$ exactly in order for diffraction to occur. The shape factor intensity $\mathcal{S}^*\mathcal{S}(\Delta\mathbf{k})$serves in effect to broaden the reciprocal lattice points. With a crystal oriented near a zone axis, that is, along a direction parallel to the line of intersection of a set of crystal planes, the Ewald sphere passes through many of these small volumes around the reciprocal lattice points, and many diffracting spots are observed. Figure 3 provides an example of Ewald sphere constructions for two orientations of the specimen with respect to $\mathbf{k}_0$, together with their corresponding selected-area diffraction (SAD) patterns. Figure 3 is drawn as a 2D slice (the x–z plane) of Figure 2. The crystal on the right is oriented precisely along a zone axis, but the crystal on the left is not.

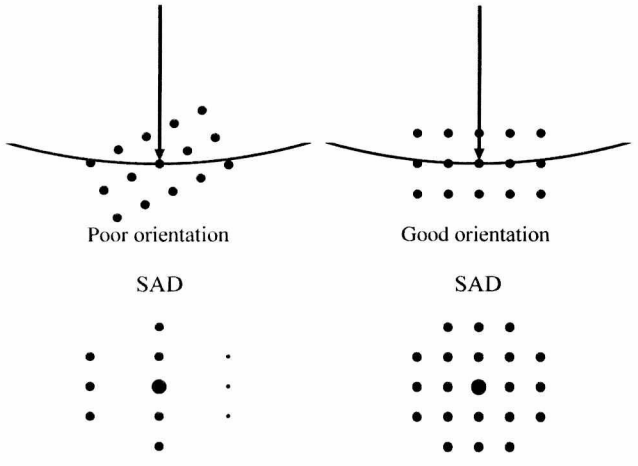

Figure 3. Two orientations of reciprocal lattice with respect to Ewald sphere and corresponding SAD patterns.

Deviation Vector and Deviation Parameter

From the previous discussion, it is apparent that the diffracted intensity observed in an electron diffraction pattern depends on exactly how the Ewald sphere cuts through the diffracted intensity around the Bragg position. To locate the exact position of intersection, we introduce a new parameter, the deviation vector $\mathbf{s}$, defined as

$$\mathbf{g} = \Delta\mathbf{k} + \mathbf{s} \tag{11}$$

where $\mathbf{g}$ is a reciprocal lattice vector and $\Delta\mathbf{k}$ is the diffraction vector whose end lies on the Ewald sphere ($\Delta\mathbf{k} = \mathbf{k} - \mathbf{k}_0$). For high-energy electrons, the shortest distance between the Ewald sphere and a reciprocal lattice point $\mathbf{g}$ is parallel to the $\mathbf{z}$ direction, so we often work with only the magnitude of $\mathbf{s}$, that is, $|\mathbf{s}| = s$, referred to as the deviation parameter. We choose a sign convention for s that is convenient when we determine s by measuring the positions of Kikuchi lines (Kikuchi, 1928). Positive s means that $\mathbf{s}$ points along positive $\mathbf{z}$. (By convention, $\mathbf{z}$ points upward toward the electron gun.) Figure 4 shows that s is positive when the reciprocal lattice point lies inside the Ewald sphere and negative when the reciprocal lattice point lies outside the sphere.

The parameter s is useful because it is all that we need to know about the diffraction conditions to calculate the kinematical shape factor. Using Equation 11 for $\Delta\mathbf{k}$ in Equation 7 yields

$$\mathcal{S}(\Delta\mathbf{k}) = \sum_{\mathbf{r}_g} \exp(-i2\pi\mathbf{g}\cdot\mathbf{r}_g)\exp(+i2\pi\mathbf{s}\cdot\mathbf{r}_g) \tag{12}$$

$$\mathcal{F}(\Delta\mathbf{k}) = \sum_{\mathbf{r}_k} f_{at}(\mathbf{r}_k, \Delta\mathbf{k})\exp(-i2\pi\mathbf{g}\cdot\mathbf{r}_k)\exp(+i2\pi\mathbf{s}\cdot\mathbf{r}_k) \tag{13}$$

$$\mathcal{F}(\Delta\mathbf{k}) \cong \sum_{\mathbf{r}_k} f_{at}(\mathbf{r}_k, \Delta\mathbf{k})\exp(-i2\pi\mathbf{g}\cdot\mathbf{r}_k) = \mathcal{F}(\mathbf{g}) \text{ or } \mathcal{F}_g \tag{14}$$

where we made the last approximation for the structure factor $\mathcal{F}(\mathbf{g})$ because $\mathbf{s}\cdot\mathbf{r}_k$ is small when the unit cell is small. Since $\mathbf{g}$ is a reciprocal lattice vector, $\exp(-i2\pi\mathbf{g}\cdot\mathbf{r}_g) = 1$ for all $\mathbf{r}_g$, which simplifies the shape factor to

$$\mathcal{S}(\Delta\mathbf{k}) = \mathcal{S}(\mathbf{s}) = \sum_{\mathbf{r}_g} \exp(+i2\pi\mathbf{s}\cdot\mathbf{r}_g) \tag{15}$$

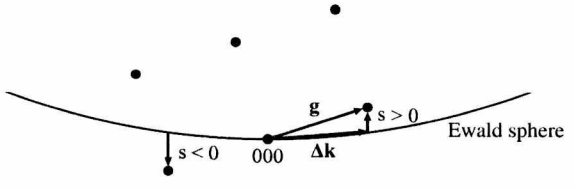

Figure 4. Convention for defining deviation vector $\mathbf{s}$ and deviation parameter s, from Ewald sphere to reciprocal lattice spot $\mathbf{g}$.

and the diffracted wave $\psi(\mathbf{g}, \mathbf{s})$, which is a function of the reciprocal lattice vector and deviation parameter, becomes

$$\psi(\mathbf{g}, \mathbf{s}) = \mathcal{F}_{\mathbf{g}} \sum_{\mathbf{r}_{\mathbf{g}}} \exp(+i2\pi \mathbf{s} \cdot \mathbf{r}_{\mathbf{g}}) \tag{16}$$

The shape factor depends only on the deviation vector $\mathbf{s}$ and not on the particular reciprocal lattice vector $\mathbf{g}$. When we substitute for the components of $\mathbf{s}$ and $\mathbf{r}_{\mathbf{g}}$ along the x, y, and z axes, we obtain an equation for the shape factor intensity that is similar to Equation 8:

$$\mathcal{S}^*\mathcal{S}(\mathbf{s}) = \frac{\sin^2(\pi s_x a_x N_x)}{\sin^2(\pi s_x a_x)} \frac{\sin^2(\pi s_y a_y N_y)}{\sin^2(\pi s_y a_y)} \frac{\sin^2(\pi s_z a_z N_z)}{\sin^2(\pi s_z a_z)} \tag{17}$$

For high-energy electron diffraction, we can make the following simplifications: (1) the deviation vector is very nearly parallel to the z axis, so s_z is simply equal to s; (2) the denominator is given as $(\pi s_z)^2$; and (3) the quantity $a_z N_z$ is the crystal thickness t. Ignoring the widths along x and y of the diffracting columns, a useful expression for the shape factor intensity is

$$\mathcal{S}^*\mathcal{S}(s) = \frac{\sin^2(\pi s t)}{(\pi s)^2} \tag{18}$$

Combining Equations 14 and 18 then gives the resulting diffracted intensity for the vector $\mathbf{g}$:

$$\mathrm{I}_{\mathbf{g}} = |\psi(\mathbf{g}, \mathbf{s})|^2 = |\mathcal{F}(\mathbf{g})|^2 \frac{\sin^2(\pi s t)}{(\pi s)^2} \tag{19}$$

This intensity depends only on the diffracting vector $\mathbf{g}$ and the deviation parameter s. Below we present many examples of how $\mathrm{I}_{\mathbf{g}}$ depends on the deviation parameter s and the sample thickness t. The dependence of $\mathrm{I}_{\mathbf{g}}$ on the position (x, y) of the diffracting column provides diffraction contrast in bright-field (BF) or dark-field (DF) images. In a two-beam condition, where only the incident beam and one diffracting beam have appreciable intensity, the intensities of the transmitted beam I_0 and diffracted beam $\mathrm{I}_{\mathbf{g}}$ are complementary, and with the incident intensity normalized to 1, we have the relationship

$$\mathrm{I}_0 = 1 - \mathrm{I}_{\mathbf{g}} \tag{20}$$

The kinematical diffraction theory developed above is valid when the intensity of the diffracted beam is much less than the transmitted beam, or

$$\mathrm{I}_{\mathbf{g}} \ll \mathrm{I}_0 \tag{21}$$

When this condition is not satisfied, one must resort to the dynamical theory of electron diffraction (Dynamical diffraction; Hirsch et al., 1977; Williams and Carter, 2009). Equations 19–21 tell us that, for a foil of constant thickness t, we expect the intensities of the transmitted and diffracted beams to vary with depth in the foil and the period of depth variation is approximately s^{-1}. This behavior is illustrated schematically in Figure 5a. The larger is the deviation parameter, the smaller is the period of oscillation and vice versa.

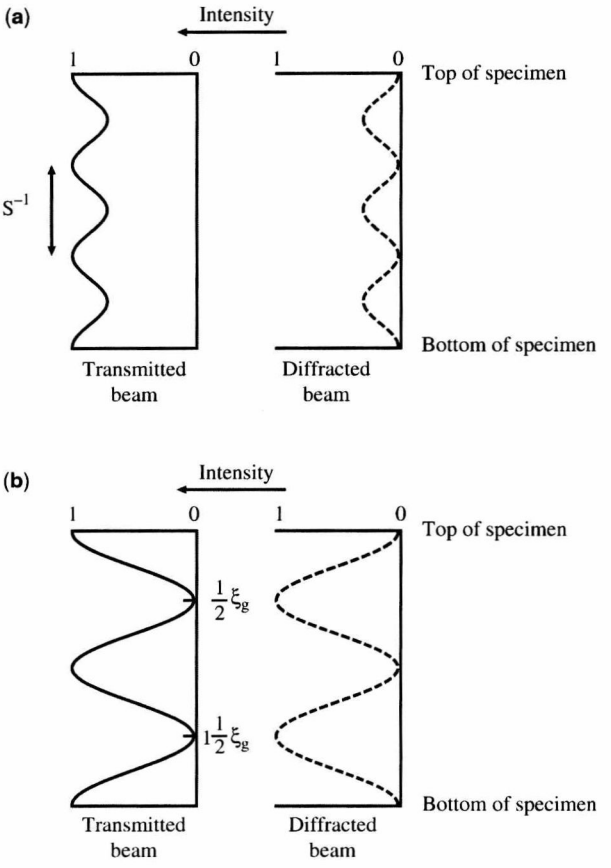

Figure 5. Extinction distance and amplitudes of transmitted and diffracted beams for two-beam condition in relatively thick crystal **(a)** under kinematical conditions with $s \gg 0$ and **(b)** under dynamical conditions with $s = 0$. (Redrawn after Edington, 1974.)

Extinction Distance

A more general way of writing Equation 19 is

$$\mathrm{I}_{\mathbf{g}} = \left(\frac{\pi}{\xi_{\mathbf{g}}}\right)^2 \frac{\sin^2(\pi s t)}{(\pi s)^2} \tag{22}$$

where the extinction distance $\xi_{\mathbf{g}}$ is given by the expression

$$\xi_{\mathbf{g}} = \frac{\pi V \cos\theta}{\lambda \mathcal{F}_{\mathbf{g}}} \tag{23}$$

and V is the volume of the unit cell, θ is the Bragg angle for the diffraction vector $\mathbf{g}$, λ is the electron wavelength, and $\mathcal{F}_{\mathbf{g}}$ is the structure factor for the diffracting vector $\mathbf{g}$. Note that $\xi_{\mathbf{g}}$ increases with increasing order of diffracting vectors because $\mathcal{F}_{\mathbf{g}}$ decreases as θ increases.

The quantity $\xi_{\mathbf{g}}$ defined in Equation 23 is an important length scale in the kinematical and dynamical

Table 1. Extinction Distances $\xi_{\mathbf{g}}$ (nm) for fcc Metals with 100-kV Electrons (from Hirsch et al., 1977)

Diffracting Plane	Al	Ni	Cu	Ag	Pt	Au	Pb
111	55.6	23.6	24.2	22.4	14.7	15.9	24.0
200	67.3	27.5	28.1	25.5	16.6	17.9	26.6
220	105.7	10.9	41.6	36.3	23.2	24.8	35.9
311	130.0	19.9	50.5	43.3	27.4	29.2	41.8
222	137.7	52.9	53.5	45.5	28.8	30.7	43.6
400	167.2	15.2	65.4	54.4	34.3	36.3	50.5
331	187.7	74.5	74.5	61.1	38.5	40.6	55.5
420	194.3	77.6	77.6	63.4	39.8	42.0	57.2
422	219.0	89.6	89.7	72.4	45.3	47.7	63.8
511	236.3	98.3	98.5	79.2	49.4	51.9	68.8
333	236.3	112.0	112.6	90.1	55.8	58.7	77.2
531	279.8	119.6	120.6	96.4	59.4	62.6	82.2
600	285.1	122.1	123.2	98.4	60.6	63.8	83.8
442	285.1	122.1	123.2	98.4	60.6	63.8	83.8

theories of electron diffraction. The extinction distance is defined as twice the distance in the crystal over which 100% of the incident beam is diffracted when $s = 0$ and the Bragg condition is satisfied exactly. The magnitude of $\xi_{\mathbf{g}}$ depends on the atomic form factors; the stronger the scattering, the shorter is $\xi_{\mathbf{g}}$. Table 1 shows some values of $\xi_{\mathbf{g}}$ for different diffracting planes in pure metals with a face-centered cubic (fcc) crystal structure (Hirsch et al., 1977). Notice how $\xi_{\mathbf{g}}$ increases with the indices of the diffracting vectors *hkl* and decreases with increasing atomic number. The values of $\xi_{\mathbf{g}}$ generally range from a few tens to a few hundred nanometers.

The extinction distance defines the depth variation of the transmitted and diffracted intensities in a crystal when the diffraction is strong. The extinction distance $\xi_{\mathbf{g}}$ applies to the dynamical situation where $s = 0$, as illustrated in Figure 5b, not just the kinematical situation where $s \gg 0$. In the development of the dynamical theory of electron diffraction, the dependence of the diffracted intensity on the deviation parameter and sample thickness is much the same as in Equation 22 with the following modification: The extinction distance in Equation 23 is made dependent on s by transforming $\xi_{\mathbf{g}}$ into an effective extinction distance, ξ_{geff},

$$\xi_{\mathrm{geff}} = \frac{\xi_{\mathbf{g}}}{\sqrt{1 + s^2 \xi_{\mathbf{g}}{}^2}} \tag{24}$$

and another quantity known as the effective deviation parameter is defined as

$$s_{\mathrm{eff}} = \sqrt{s^2 + \xi_{\mathbf{g}}{}^{-2}} \tag{25}$$

Equation 24 shows that the effective extinction distance $\xi_{\mathrm{geff}} = \xi_{\mathbf{g}}$ when $s = 0$, but ξ_{geff} decreases with increasing deviation from the exact Bragg position. With large deviations, $s \gg 1/\xi_{\mathbf{g}}$, and $\xi_{\mathrm{geff}} = s^{-1}$, so the kinematical result is recovered for large s.

Diffraction Contrast from Lattice Defects

The following are important variables in the diffraction contrast from defects in crystals:

$\mathcal{F}(\mathbf{g}) \equiv$ structure factor of unit cell
$t \equiv$ specimen thickness
$\Delta\mathbf{k} \equiv$ diffraction vector
$\mathbf{g} \equiv$ reciprocal lattice vector
$\mathbf{s} \equiv$ deviation vector ($\mathbf{g} = \Delta\mathbf{k} + \mathbf{s}$)
$\mathbf{r} \equiv$ actual atom centers
$\mathbf{R} \equiv$ atom centers in a perfect crystal ($\mathbf{R} = \mathbf{r_g} + \mathbf{r_k}$,

where $\mathbf{r_g}$ refers to the lattice and $\mathbf{r_k}$ to the basis)

$\delta\mathbf{r} \equiv$ displacements of atoms off the ideal atom centers ($\mathbf{r} = \mathbf{R} + \delta\mathbf{r}$).

Note that the actual atom centers $\mathbf{r}$ as defined above are the locations of the atoms off of the atom positions in a perfect crystal $\mathbf{R}$ that are given by the lattice (plus basis) points, that is, the ideal mathematical positions. Spatial variations in these variables (e.g., an x dependence) can produce diffraction contrast in an image. Examples include the following:

$\mathcal{F}$: $d\mathcal{F}/dx$ causes chemical (compositional) contrast,
t: dt/dx causes thickness contours,
$\mathbf{g}$: $\mathrm{d}\mathbf{g}/\mathrm{d}x$ causes bend contours,
s: $\mathbf{d}s/\mathbf{d}x$ causes bend contours, and
$\delta\mathbf{r}$: $\mathbf{d}\delta\mathbf{r}/\mathbf{d}x$ causes strain contrast.

Up to this point, we have only considered diffraction occurring from perfect crystals. We now consider the displacements in atom positions $\delta\mathbf{r}$ caused by strain fields around defects in a crystal. These displacements represent the time-averaged position of the atoms during electron scattering. We decompose r into components from the lattice vectors, basis vectors, and distortion